Dynamic Response of Q460 High-Strength Steel Beams Under Near Explosive Loading

Xiuhua Zhang, Yalin Guan, Weijia Zhang

Abstract—**The study of the explosion resistance of high-strength steels has become increasingly significant with their increasing use in engineering. In this study, the dynamic response and failure mode of high-strength welded I-shaped steel beams fixed at both ends under near-explosive loading was investigated using finite element (FE) analysis software ANSYS/LS-DYNA and the fluid–structure coupling method. Using the parametric research approach, the dynamic responses of steel beams with different scaled distances were examined. Additionally, the study explored the function of the floor slab in the failure process of the steel beam. The explosion shock wave acted on the steel beam as a spherical wave. The steel beam reached twice the ultimate strain at the lower flange and maximum deflection and strain at the mid-span and support, respectively. Welded composite I-beams fixed at both ends might experience flexural-shear failure, local buckling failure of the flange, and lateral flexural-torsional buckling failure when subjected to explosive loading at different scaled distances. The effect of floor slabs was considered under different scaled distances, the upper floor slab and concrete splash of the floor slab protected the steel beam, and the displacement is reduced by 56.7%, which underwent slight flexural – torsional failure.**

Index Terms—**explosive loading, failure mode, high-strength steel beams, upper floor action**

I. Introduction

In recent years, building collapses have occurred due to explosions. Damage to a steel beam, the primary stress element in the steel structure of a building, likely results in local damage or even lead to the complete collapse of the building structure. High-strength steel is increasingly utilized in the construction of steel structures owing to its superior stress performance, economic advantages, and sustainability [1]. Therefore, investigation of the explosion resistance of high-strength steel beams is crucial.

The propagation and characterization of explosive shock waves significantly affect the investigation of structural explosive resistance, serving as a foundational reference for the arrangement of munitions in experimental and numerical simulations. This in turn facilitates the development of models for precise explosion analysis [2], [3]. As the number of component simulations under explosive loading continues to increase, several domestic and global studies have been conducted on the dynamic responses and explosion resistances of differently stressed components. Zhou et al. [4] utilized the SPH method for blasting vibration in their secondary development of LS-DYNA, suggesting a combination of SPH for the near zone and FEM for the far zone. Dinu et al. [5] conducted experiments involving explosion shock wave loading on the weak axis of a steel frame substructure and performed a finite element (FE) analysis. The analysis revealed that the column webs suffered impulsive shearing at the instant of the explosion, leading to a complete loss of the gravity load-carrying capacity. In a separate study, Hu et al. [6] examined the impact of several explosive loads on the stability of cylindrical shells. Their analysis revealed that the explosive resistances of double-layer cylindrical shells with reduced rib spacing were comparable under lower explosive loads. However, this resistance decreased as the explosive load increased. Zhao et al. [7] conducted a parametric analysis of double-corrugated steel plate concrete composite slabs subjected to contact explosions. They compared the failure and maximum midspan displacement of different types of corrugated specimens and found that double-corrugated steel-plate concrete floor slabs exhibited smaller midspan deflections and superior explosive resistance. Mohammad et al. [8], [9], [10] numerically investigated H-beam columns under explosive loading using experiments and FE simulations to derive failure assessment equations. Arafa et al. [11], [12] used an ANSYS/LS-DYNA simulation to investigate the impact of boundary conditions and web shape on the toughness of steel beams with open webs under explosive loading. They proposed a damage index for steel beams with open webs, and demonstrated that the shape of the web openings significantly affected the dynamic characteristics of the beams. Guruprasad et al. [13] [14] conducted experimental studies on laminated structures comprising thin steel plates subjected to explosive loading. Their findings revealed that the laminated structure exhibited enhanced energy absorption, a dissipative effect on the explosive shock wave, and a prolonged collapse time. The damage performance of beams, columns, and reinforced concrete beams under explosive loading was investigated [15], [16], [17], [18]. Single- and multiple-degree-of-freedom models were used to predict the displacements and strains and analyze the strength and stability of the elements. It was concluded that the single-DOF model was the most effective for predicting the kinetic response of the elements in the elastic and inelastic phases. Yang et al. [19] analyzed a rational anti-explosion model for exploded steel frame columns and derived a theoretical calculation method for the end restraints of such columns. Additionally, Zhang et al. [20] examined the effect of geometry on the deformation and

Manuscript received January 20, 2025; revised July 17, 2025.

Xiuhua Zhang is a professor of Civil Engineering and Transportation, Northeast Forestry University, Harbin 150040, China (e-mail: zhangxh2000@163.com).

Yalin Guan is a graduate student of Civil Engineering and Transportation, Northeast Forestry University, Harbin 150040, China (e-mail: 13995131076@163.com).

Weijia Zhang is a graduate student of Civil Engineering and Transportation, Northeast Forestry University, Harbin 150040, China (e-mail: 1274107556@qq.com).

damage of steel plates under restricted explosive loading and demonstrated that preformed holes could mitigate the peak pressure from secondary shock waves. ANSYS/LS-DYNA was used to parametrically analyze the influencing factors of explosive resistance effects for steel frame columns and welded I-beams under different explosive loads [21], [22], [23]. Their findings revealed a continuous collapse process for steel-frame structures under the combined effects of explosive air shock waves and seismic waves. Zhou et al. [24] performed a numerical analysis of H-shaped steel columns subjected to different proportional distances of explosive loads and concluded that an enhanced protection of the middle section of the column is essential in the explosion-resistant design of steel columns. Arafa and Nawar et al. [25], [26] conducted numerical analyses of the dynamic responses of steel columns with openings under different explosive loads using ANSYS and LS-DYNA. Hu et al. [27] investigated the near-field explosion resistance of steel-box beams using LS-DYNA to determine their explosive damage characteristics. Yu et al. [28] performed a numerical analysis of the near-field explosion conditions of building column surfaces to discuss the distribution of the explosive load at different scaled distances, proportional explosive heights, explosive equivalent of the explosive load distribution, and duration of the positive phase overpressure. The column explosive load on the surface was simplified into a triangular load model to derive a formula for calculating the duration of positive-phase overpressure. Xiao et al. [29] investigated the effects of different incident angles on the explosive load and dynamic response of steel columns. An et al. [30] employed numerical simulations to study concrete's dynamic response to explosive loading. They found that integrating the Holmquist-Johnson- Cook and Jones-Wilkens- Lee models can accurately simulate concrete's behavior during explosions. The simulation outcomes offer a thorough understanding of the fracture and crushing mechanisms in concrete.

Extensive research has been conducted on the behavior of structural steel members under explosive loads. However, investigations on the impact of Q460 high-strength steel on the explosive resistance of steel beams remain incomplete. Therefore, it is important to examine the response of high-strength steel beams to explosive loads. In this study, the explicit dynamic FE software ANSYS/LS-DYNA was used with a fluid–structure coupling calculation method to analyze the effect of explosion shock waves on high-strength welded I-shaped steel beams. Furthermore, the dynamic response and damage patterns of high-strength steel beams with fixed supports at both ends were investigated, and the variation rules of pressure, displacement, and strain during the damage process were ascertained. An analysis of the effects of different proportional distances and flange widths on explosive performance was carried out. This study investigated how an upper-floor slab affected a steel beam under explosive shock, aiming to lay the groundwork for evaluating the explosive resistance of beam and plate structures in steel buildings.

II. Verification and Establishment of FE Models

LS-DYNA was used to perform a numerical analysis of the failure mode and dynamic response of a high-strength steel beam with fixed supports at both ends. Additionally, a fluid–structure coupling relationship was established by considering the strain rate effect of steel. The results of the steel-column explosion experiment and numerical simulation were compared to validate the feasibility of the FE method and reliability of the parameters.

A. Model unit types and material parameters

1. Types of units

A SHELL163 shell element was used for steel, and a SOLID164 solid element was used for the explosives, concrete, and air.

The SHELL163 element has bending and membrane features, allows the application of planar and normal loads, and is suitable for all nonlinear characterizations in explicit dynamics analyses [31]. In the dynamic response calculation, the solid164 element was used to reduce the effects of large deformations by increasing the viscous resistance of the hourglass, and the keyword *CONTROL_HOURGLASS was added to define the hourglass control [32].

2. Steel materials

In this study, the *MAT_PLASTIC_KINEMATIC plastic kinematic hardening model was used to simulate the behavior of steel. Cowper–Symonds model was used to consider the effect of strain rate on strength. The basic parameters of the steel used in the numerical validation and simulation are listed in Table I [33]. The kinematic hardening effect of a material can be expressed as follows:

$$\sigma_{\mathrm{d}} = [1+(\frac{\dot{\varepsilon}}{n})^{\frac{1}{P}}](\sigma_{\mathrm{y}} + \beta E_{\mathrm{m}} \varepsilon_{\mathrm{m}}^{\mathrm{eff}}) \tag{1}$$

where σ_{y} and σ_{d} denote the static yield stress and dynamic yield stress, respectively, $\dot{\varepsilon}$ denotes the strain rate, n and P denote strain rate parameters, β denotes the hardening parameter, $\varepsilon_{\mathrm{m}}^{\mathrm{eff}}$ denotes the equivalent plastic strain, and $E_{\mathrm{m}} = E_{\tan}E/(E-E_{\tan})$ denotes the plastic strengthening modulus.

TABLE I
Material Parameters of Steel

Steels	FE Verification (Q235)	Q460
E (MPa)	2×10^5	2×10^5
Poisson's ratio	0.3	0.3
Mass density (kg/m^3)	7850	7850
Yield stress (MPa)	235	460
β	0	0
γ	40	1234
P	5	4.15
$E_{\tan}$ (MPa)	0.6×10^3	0.9×10^3
Failure strain	0.20	0.17

3. Explosive materials

The material model used for the TNT explosive is *MAT_HIGH_EXPLOSIVE_BURN, and the corresponding equation of state is *EOS_JWL. The keyword *INITIAL_ DETONATION defines the material and location where the explosion occurs and the time of detonation of the explosion. The explosive parameters are listed in Table II and are expressed as follows [33]:

$$p = A_1\left[1-\frac{\omega}{R_1 V}\right]e^{-R_1 V} + B_1\left[1-\frac{\omega}{R_2 V}\right]e^{-R_2 V} + \frac{\omega E}{V} \tag{2}$$

where p denotes the pressure of the detonation product, V

denotes the relative volume, E denotes the internal energy per unit volume, and 7 GJ/m^3 was taken for this study, and ω, A, B, R_1, and R_2 are material constants.

TABLE II
MATERIAL PARAMETERS OF TNT EXPLOSIVE

ρ/(kg/m^3)	D/ (M/S)	P_{CJ}/ GPA	A_1/ GPA	B_1/ GPA	R_1	R_2	ω
1630	6930	21.0	371.2	3.231	4.15	0.95	0.35

4. Air material

A multimaterial model *MAT_NULL was used to define air using the *EOS_LINEAR_POLYNOMIAL equation of state, which accurately characterizes the mechanical properties of the fluid-material model through the following expression:

$$P = C_0 + C_1\mu + C_2\mu^2 + C_3\mu^3 + (C_4 + C_5\mu + C_6\mu^2)E \quad (3)$$

where C_0, C_1, C_2, C_3, C_4, C_5, and C_6 are the parameters of the equation of state with C_1, C_2, C_3 and C_6 were 0, E denotes the current internal energy. Furthermore, in equation $\mu = \rho / \rho_0 - 1$, ρ denotes the current density and ρ_0 denotes the initial density. These values are listed in Table III.

TABLE III
MATERIAL PARAMETERS FOR AIR.

ρ/(kg/m^3)	C_0/PA	C_4	C_5	E (J/m^3)	V_0
1.29	-1 × 10^5	0.4	0.4	2.5 × 10^5	1.0

5.Concrete materials

*MAT_JOHNSON_HOLMQUIST_CONCRETE (HJC) material model was used for concrete. The material parameters of the C50 concrete used in the simulation are listed in Table IV. The constitutive equation for the model is as follows:

$$\sigma^* = [A(1-D) + Bp^{*N}][1 + C\ln(\dot{\varepsilon}^*)] \quad (4)$$

where A denotes the dimensionless bond strength, B denotes the dimensionless pressure hardening coefficient, C denotes the strain rate coefficient, σ^* denotes the dimensionless equivalent stress, $\dot{\varepsilon}^*$ denotes the dimensionless strain rate, and p^* denotes the dimensionless pressure .

TABLE IV
HJC CREEP PARAMETERS FOR C50 CONCRETE

ρ/(kg/m^3)	A	B	C	N	$f_c^{'}$/GPa	N_{max}	D_1	D_2
2440	0.79	1.6	0.007	0.61	0.048	7.0	0.04	1.0

B. Finite element model verification

Grisaro et al. [34] conducted experiments to obtain a charge weight of 5138 g, with a cubic charge measuring 147.6 mm × 147.6 mm × 147.6 mm, under a close-range air explosion load at a detonation distance of 500 mm. The deformation and failure modes of a fixed steel column were examined using a welded I-shaped cross-sectional steel column with dimensions of 140 mm × 133 mm × 5.5 mm × 8.5 mm. The model size selected in this study is consistent with that of a strong shaft specimen without a stiffener subjected to an explosion shock wave, as previously described [34]. The established FE model is shown in Fig. 1. The mesh sizes of the explosive, air, and steel columns were 25, 50, and 50 mm, respectively. The mesh sizes of the air and explosives were validated for FE analysis in the literature[35]. This study focused on simulating the dynamic response of a steel column to short-range explosions. Fig. 2 illustrates the deformation of the steel in the experiment and validates the steel column deformation via FE simulation. Fig. 2 shows that the FE simulation was consistent with the experimental steel column deformation, with buckling occurring at the flange of the steel column facing the explosion. The measured deformation range in the experiment was 620 mm, whereas that in the numerical simulation was 612 mm, demonstrating good agreement between the two. Fig. 3 illustrates the displacement–time curve of the steel column web displacement, demonstrating that the residual displacement of the numerical simulation curve aligned with the experimental value. The component discussed in literature [34] was not subjected to an axial force and could be considered a flexural component. The FE simulation and experimental phenomena exhibited good agreement, providing a solid foundation for the subsequent analysis.

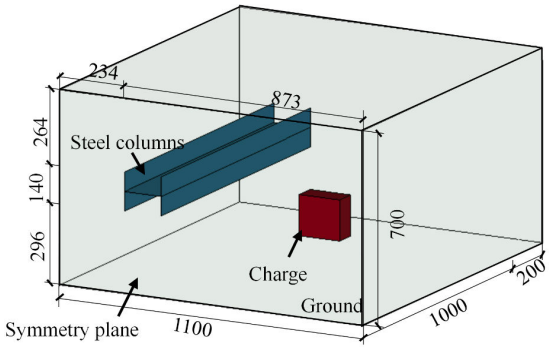

Fig. 1. FE model of the experiment (Unit: mm).

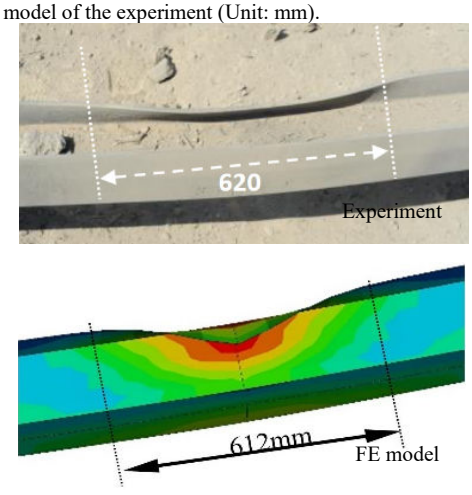

(a) Comparison of local deformation

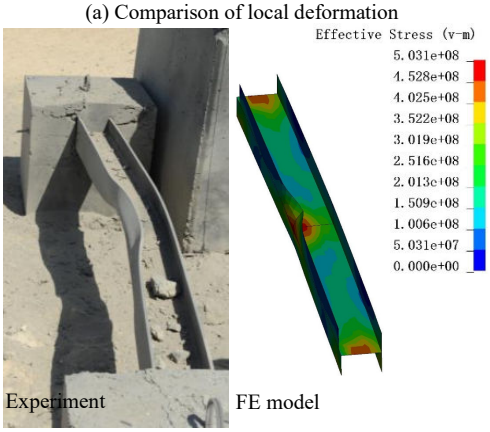

(b) Comparison of overall deformation

Fig. 2. Comparison between experimental and FE simulations.

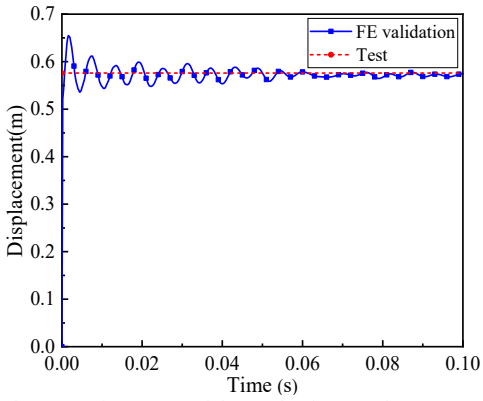

Fig. 3. Displacement time curve of the steel column web.

C. *Establishment of FE model for steel beam*

As illustrated in Fig. 4(a), the subject of this study was a steel beam in a 3-layer 2-span steel frame structure. The steel beam had a welded I-section cross-section measuring 420 mm × 200 mm × 10 mm × 14 mm with a span of 6 m and was made of Q460 steel. Both ends of the steel beam were fixed, and all the degrees of freedom at both ends of the support were constrained. Based on actual working conditions and calculations following the "Load Code for Design of Building Structures" [36], the superstructure of the steel beam transmits a static load of 103.6 kN, which is converted into a mean distributed load of 85.5 kN/m².Airspace dimensions were 2.4 m × 5.5 m × 3.5 m, with explosives measuring 400 mm × 400 mm × 400 mm, and a TNT equivalent of 104.32 kg. The distance from the center of the explosives to the midspan of the upper flange of the steel beam was *R*, and the explosives were detonated at the center. As shown in Fig. 4(b), a 1/2 model was used in the analysis to reduce the computation time and improve the computational efficiency. Symmetric boundary conditions were imposed on the symmetry plane, while non-reflective boundary conditions were applied to other surfaces to simulate infinite-domain analysis.

The steel beam was SHELL163, and the explosives and air were SOLID164, with mesh sizes of 25 mm for the explosives and 50 mm for the air and steel beams. A fluid–structure coupling algorithm was used to simulate the impact response of the explosion shock wave. Air and explosives were modeled using a Euler mesh, the elements used a multimaterial arbitrary Lagrange (ALE) algorithm, and the steel was modeled using a Lagrange mesh.

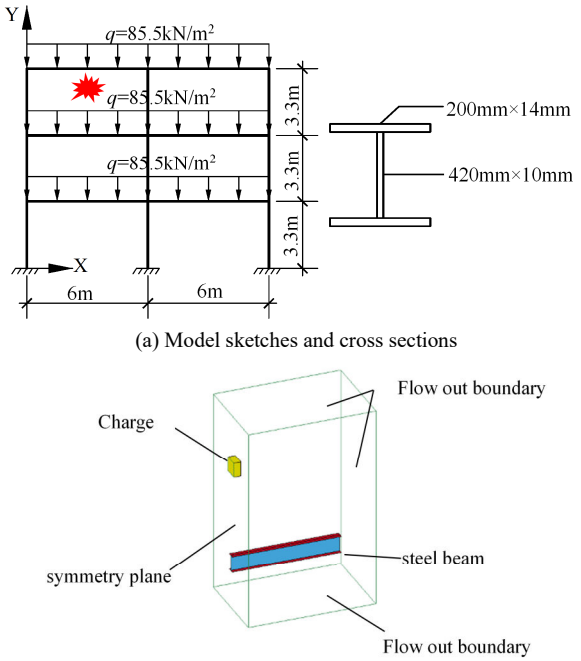

(a) Model sketches and cross sections

(b) Computational model

Fig. 3. Schematic of welded I-beam model

III. Dynamic Response of Steel Beam

To study the explosion shock wave spreading patterns in free air and steel beams, the pressure, displacement response, and strain of the steel beams were analyzed using a constant charge and proportional distance $Z = 0.53$ m/kg$^{1/3}$.

A. *Propagation law of explosive shock waves in steel beam*

Fig. 5 shows the propagation of an explosion shock wave on a steel beam. At the onset of the explosion at $t = 0.265$ ms, the gases produced by the explosion expanded rapidly, creating a spherical wave that propagated outward. At $t = 0.834$ ms, the shockwave enveloped the steel beam span, causing the beam web to experience opposite forces. The shockwaves reflected between the upper and lower flanges of the beam and resulted in a more significant failure of the flanges than that of the web. At $t = 1.784$ ms, the outermost shock wave reached a position near the support of the steel beam, thereby creating a sparse wave around the beam. This results in the support experiencing significant impact pressure, leading to plastic deformation. At $t = 2.586$ ms, as the shockwave moved forward, the upper section of the steel beam was obstructed, causing the shockwave to flow around it.

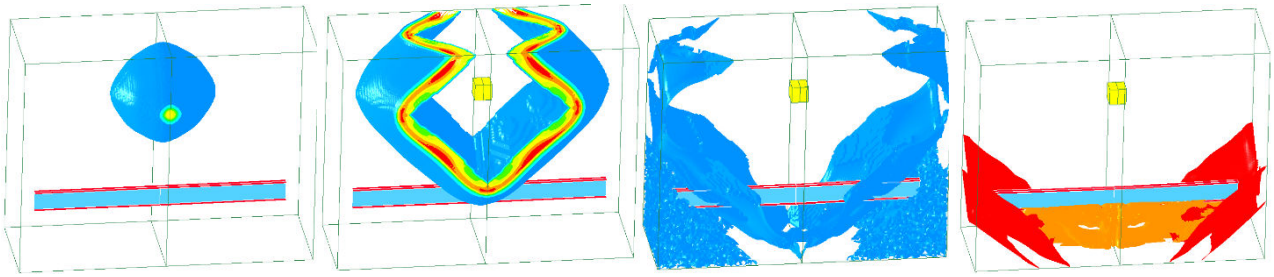

(a) $t = 0.265$ ms (b) $t = 0.834$ ms (c) $t = 1.784$ ms (d) $t = 2.586$ ms

Fig. 5. Propagation process of the explosion shock wave in a steel beam at different times.

B. *Shock wave pressure of steel beam*

Fig. 6 shows the peak pressure generation and pressure cloud diagram of the steel beam at different explosion times when $Z = 0.53$ m/kg$^{1/3}$. Fig. 7 illustrates the magnitude of the shockwave pressure experienced at different positions on the beam at different times.

Fig. 6 and Fig. 7 show that at t = 1.5 ms, which was the onset of the explosion, the shock wave reached the midpoint of the steel beam. At this position, the pressures on both the upper and lower flanges of the beam peaked, with the maximum pressure recorded at 7.89×10^7 kN. At t = 12.6 ms, a portion of the shock wave circumvented the web, the pressure at the upper flange of the span and the connected web is large, with a maximum pressure of 1.70×108kN which led to significant torsional deformation with localized buckling occurring at the support ends of the lower flange. Additionally, the upper edge experienced a downward concave deformation owing to the explosion, which resulted in local instability. At t = 23.7 ms, the shockwave was reflected between the upper and lower flanges of the steel beam, resulting in the highest pressure at these flanges, with a maximum stress of 1.67×10^8 kN. Ultimately, the steel beam experienced a relatively uniform pressure distribution, leading to concavity in the upper and lower flanges, combined with flexural and twisting in opposite directions.

In conclusion, when $Z = 0.53$ m/kg$^{1/3}$, the highest pressure on the steel beam occurred at the center of the midspan flange and gradually decreased toward the sides. The pressure was greatest at the support locations. Over time, the pressure was distributed more evenly across the beam; however, it did not decrease.

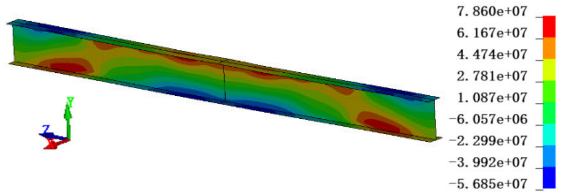

(a) t = 1.5 ms

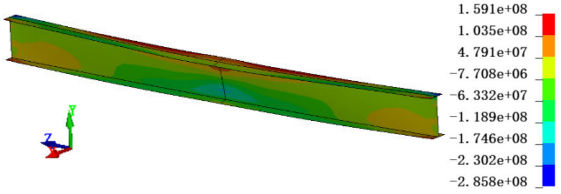

(b) t = 12.6 ms

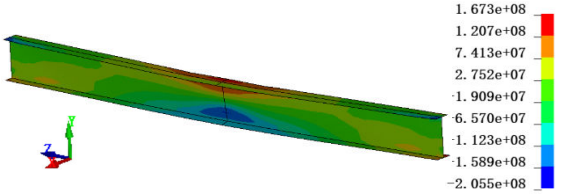

(c) t = 23.7 ms

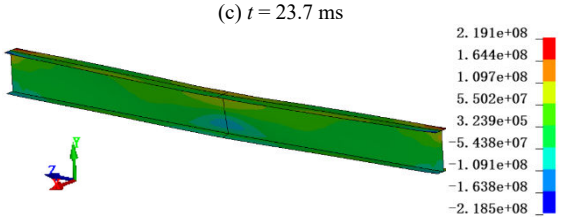

(d) t = 45.7 ms

Fig. 6. Pressure cloud of the steel beam under $Z = 0.53$ m/kg$^{1/3}$.

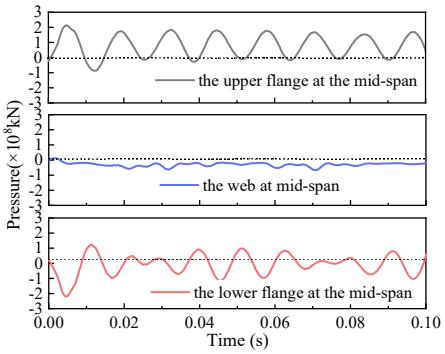

(a) Pressure– time curve at midspan.

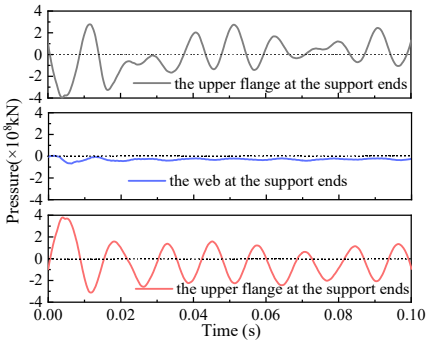

(b) Pressure–time curve at the support ends.

Fig. 7. Pressure–time curves of beam at different positions.

C. *Displacement of steel beam*

The explosive force acting on the steel beam did not spread evenly owing to the impact pressure from the explosion. Shock waves encounter several obstacles that alter their original propagation paths. Consequently, the dynamic response at different positions of the steel beam varies, and the effect of the explosion shock wave on the steel beam cannot be equated with a uniform load.

Fig. 8 shows that the greatest vertical displacement of the steel beam occurred at the midspan position, where the propagation distance was minimal. As the distance from the midspan increased on either side of the beam, the propagation path lengthened, resulting in a decrease in the shockwave overpressure. Furthermore, the vertical displacement decreased with increasing distance from the midspan. The peak vertical displacement of the steel beam was recorded at 7 ms post-explosion, with the rate of increase of the maximum displacement gradually tapering. Failure and deformation were the greatest at the location directly subjected to the peak effect of the explosion shock wave. The deformation reached its maximum value when the explosion shock wave propagated towards the steel beam. Owing to the reflection and diffraction of the shock wave, the deformation of the steel beam experienced a reverse displacement. However, it quickly returned to normal-frequency oscillation.

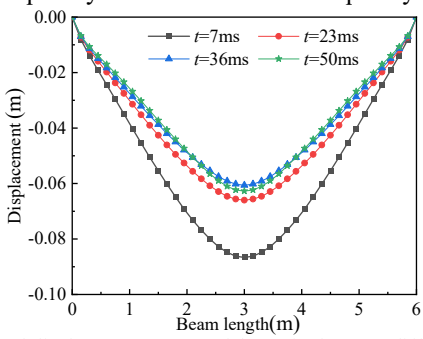

Fig. 8. Vertical displacement curves of the entire beam at different moments.

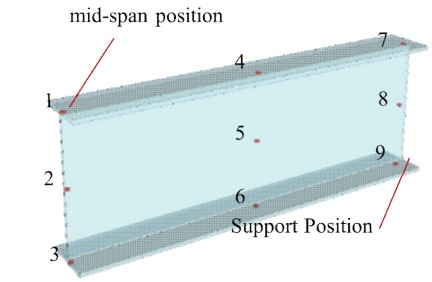

(a) Layout

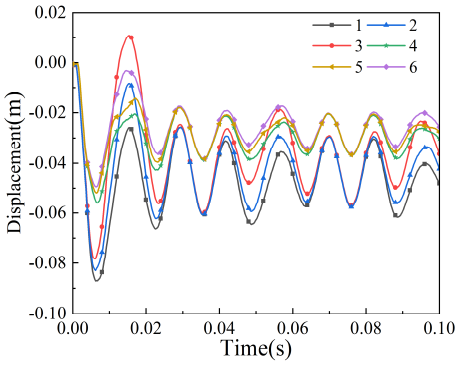

(b) Vertical displacement at 1/2 span center and 1/4 span

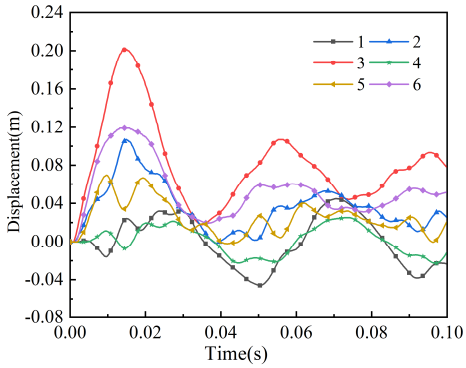

(c) Horizontal displacement at 1/2 span center and 1/4 span

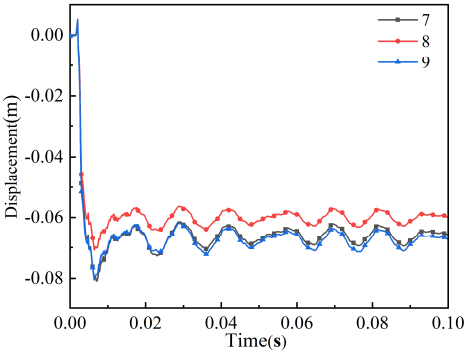

(d) Vertical displacement at support.

Fig. 9. Measurement point arrangement and displacement time–history curve.

Fig. 9(a) shows the measure point arrangement of the 1/2 steel beam model. Points were selected at the middle of the span, 1/4 span, and 0.15 m from the steel beam support at the upper flange, web center, and lower flange. As shown in Fig. 9(b), the displacement at each measurement point rapidly reaches its peak, after which it exhibits a periodic shock motion. Additionally, owing to the energy dissipation during propagation, the displacement at each point gradually decreased from top to bottom. Fig. 9(c) shows that the lateral displacement at measurement point 3 is significantly greater than the vertical displacement. The extent of distortion experienced at points 3 and 6 on both sides of the lower flange increased over time. This was primarily caused by a shock wave that traveled to the lower flange of the steel beam through diffraction and bypassing, thereby creating a tensile wave. This wave exerts an upward force on the lower flange, leading to plastic deformation in the middle of the span and generating a shock wave perpendicular to the web of the steel beam. Consequently, this resulted in lateral instability of the steel beam. Fig. 9(d) indicates that the minimum deflection was observed at measurement point 8, which was situated at the center of the web plate. Measurement points 7 and 9 exhibited nearly identical displacements because they were closer to the fixed support. Consequently, the displacement at these points was minimal, exhibiting some residual deformation, and the vibration frequencies were identical.

D. Energy Dissipation Analysis

The explosion process emits a significant amount of energy rapidly, producing intense heat and releasing gases. Consequently, understanding how energy dissipates in a steel beam impacted by an explosion is crucial. Figure 10 illustrates the energy curves for both the web and flange.

Figure 10 illustrates that when the shock wave first impacts the steel beam, the kinetic energy of the beam rises quickly, while the internal energy remains lower than the kinetic energy. This is a result of the shock wave accelerating the steel beam, leading to an increase in velocity and consequently generating kinetic energy. As time progresses, the internal energy gradually rises while the kinetic energy diminishes. This change occurs because the steel beam undergoes plastic deformation, which generates deformation energy, or internal energy. Subsequently, the kinetic energy and internal energy are constantly oscillated and transformed into each other, and the total energy tends to be stabilized. Comparing the energy curves of the web and the flange, the energy change trend is basically the same after being shocked by the shock wave, but the overall flange is larger than the web, and the comprehensive displacement analysis shows that the flange deforms more and consumes more energy.

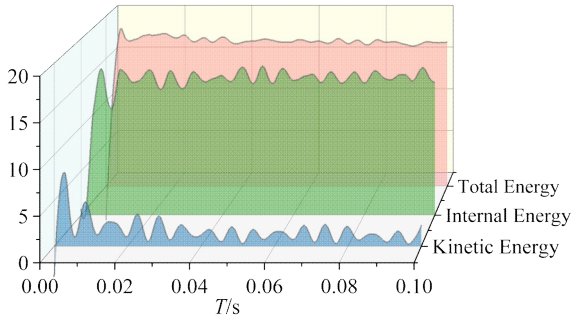

(a) Web energy time-course curve

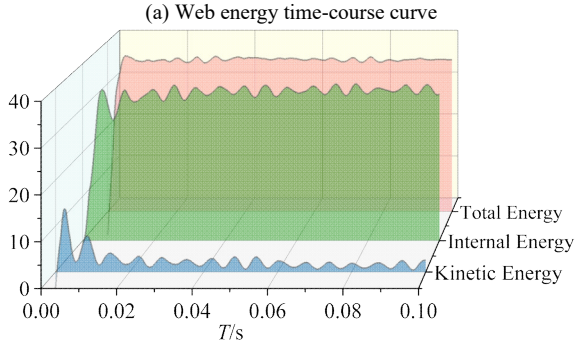

(a) Flange energy time-course curve

Fig. 10. Z=0.53m/kg$^{1/3}$ steel beam energy time-course curve

E. Strain–time history curve

The steel beams were fixed at both ends and there was no displacement at the support. This section analyses whether the support location enters plasticity by examining the strain at the support. Fig. 11 shows the plastic strain contour map at the beam support at a certain moment and the arrangement of the measurement points.

The strains at different locations were examined over time, and the resulting strain–time history curves are presented in Fig. 12, illustrating that the strain at the support reaches approximately 4% of its maximum value. The strain at the edge of measurement point 13 was the highest, exhibiting a decrease of 11.59%, which is more than twice the ultimate strain. The strains at measurement points 10 and 13, positioned along the diagonal line, were higher and quickly reached the failure strain at 5.2 and 3.8 ms, respectively. Additionally, the strain increased significantly over time. Measurement points 11 and 12 situated on opposite diagonals exhibited relatively low strains, with point 12 experiencing plasticity in the later stages.

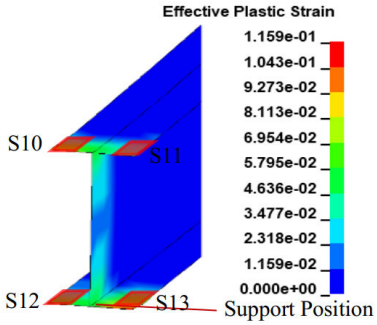

Fig. 11. Plastic strain contour diagram for the beam support

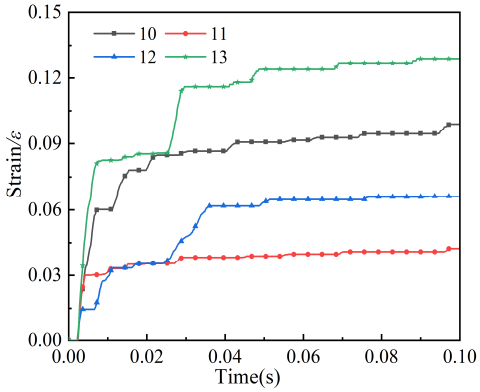

Fig. 12. Strain–time history curve at beam support.

IV. Failure Modes of Steel Beams at Different Proportional Distances

To investigate the failure modes of the steel beams, numerical simulations of explosive loads at the three distinct scaling distances, listed in Table V, are conducted to assess the failures inflicted on the steel beams during an explosion in air.

TABLE V
DIFFERENT LOADING CASES

Simulation ID	TNT equivalent /kg	Explosive distance /R (m)	Proportion distance /Z (m/kg$^{1/3}$)
Case I	104.32	2.5	0.25
Case II	0.6×10^3	1.8	0.38
Case III	0.20	1.2	0.53

A. Case I ($Z = 0.25$m/kg$^{1/3}$)

In Case I, the explosion process was rapid, the shock wave action time was short, the acceleration was significant, and the strain rate was elevated. The overall stability bearing capacity of the steel beam exhibited a more significant enhancement than the increase in the shear bearing capacity. At t = 3 ms, the lower flange and web at the midpoint of the steel beam span sustained significant shear failure owing to the shockwave. The upper section of the midspan experiences compression, whereas the lower section experiences tensile stress. Additionally, the upper flange and surrounding area exhibited cracking, resulting in the formation of a substantial deformation fold with most elements ceasing to function. At t = 10 ms, the shock wave impacted both sides of the midspan web, causing it to shear and flip out-of-plane. At t = 15 ms, the upper section of the beam continues to undergo deformation, whereas the lower flanges on both sides experience permanent plastic deformation. As shown in Fig. 13, the steel beam experiences flexural failure and a combination of flexural and shear failures.

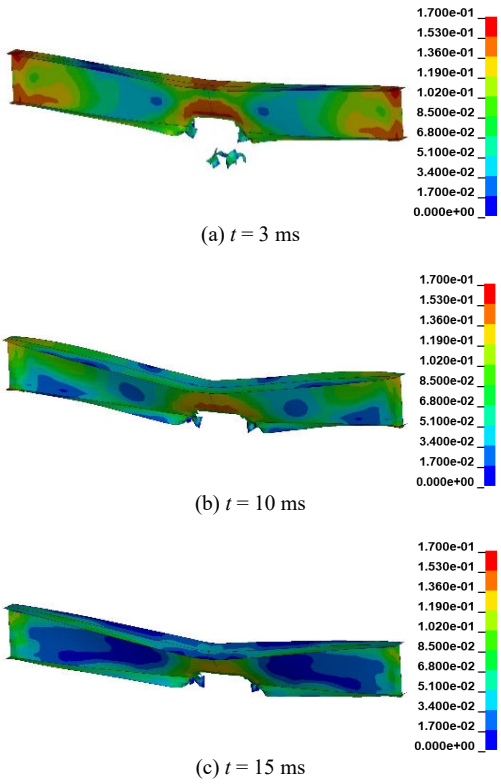

(a) t = 3 ms

(b) t = 10 ms

(c) t = 15 ms

Fig. 13. Destruction process of Case I steel beam.

B. Case II ($Z = 0.38$m/kg$^{1/3}$)

In Case II, the steel beam did not attain its ultimate bearing capacity. The explosion occurs at t = 3 ms, at which point the supports at both ends experience increased stress. The explosive impact was primarily absorbed in the midspan region, resulting in the lateral deflection of the upper flange and localized buckling of the same flange. At t = 10 ms, the explosive shock wave continued to propagate. This generated a bypass flow that acted on the web. Furthermore, the vertical and lateral displacements were similar, and the overall load-bearing capacity was maintained. Fig. 13 shows that a localized flexural failure occurred in the flange.

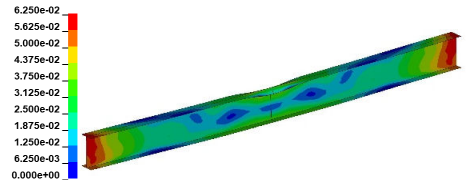

(a) t = 3 ms

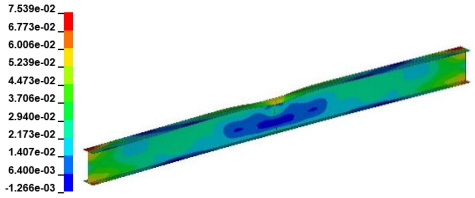

(b) t = 10 ms

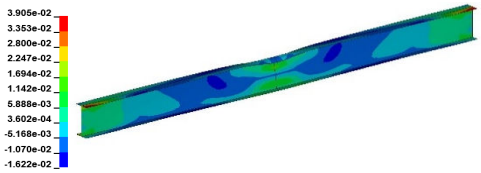

(c) t = 15 ms

Fig. 14. Destruction process of Case II steel beam

C. *Case III* ($Z = 0.53 m/kg^{1/3}$)

In Case III, as the shock wave propagated at t = 3 ms, the steel beams exhibited a certain amount of vertical deflection at their midpoint, whereas the lateral displacement remained minimal. Both the steel beam span and support yielded. At t = 10 ms, the steel beam exhibited out-of-plane instability, characterized by the flexural twisting of the upper and lower flanges in opposite directions. Overturning the upper flange induced a lateral displacement of the web. This phenomenon generated shock waves that underwent reflection and refraction, which exerted significant forces on the underside of the web and the lower flange in conjunction with the transmitted and diffracted shock waves. This led to pronounced torsional deformation in the lower flange. At t = 15 ms, the lateral displacement of the steel beam decreased, which was accompanied by a decrease in the out-of-plane torsion. The explosive process was rapid, resulting in significant deformation prior to the attainment of a stable load-bearing capacity, which ultimately led to the loss of overall stability in the steel beams. As illustrated in Fig. 15, the complete failure process was lateral flexural–torsion instability.

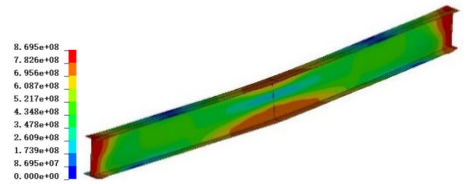

(a) t = 3 ms

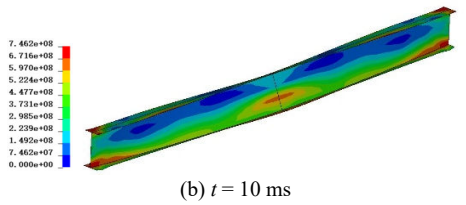

(b) t = 10 ms

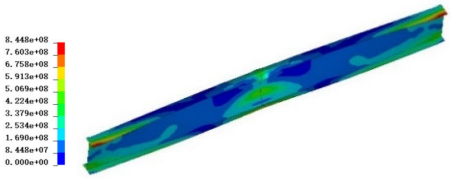

(c) t = 15 ms

Fig. 15. Destruction process of the Case III steel beam.

Fig. 16 illustrates the influence of the scaled distance from the explosive load and width of the steel flange on the maximum displacement and pressure experienced at the midspan of the steel beam. The findings indicate that the peak pressure at the midpoint of the span diminished as the proportional distance increased, which in turn led to a reduction in the maximum vertical displacement at the midspan. The highest rise in mid-span pressure and vertical displacement between Z = 0.25 m/kg$^{1/3}$ and Z = 0.53 m/kg$^{1/3}$ with a flange width of 200 mm reached 50.33% and 52.15%, respectively. A comparative analysis of Fig. 15(a) and (b) shows that the explosion load damage to the steel beams decreased with increasing flange width. Initially, the flange experiences most of the explosive load, which subsequently mitigates the flow around effect. As the scaled distance decreased, the damage to the steel beam became more severe.

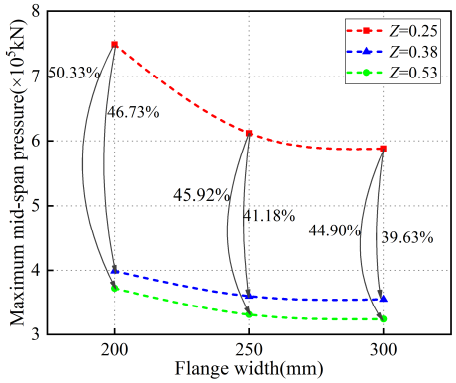

(a) Maximum mid-span pressure

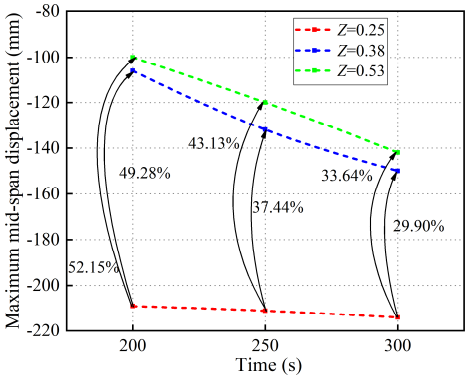

(b) Maximum mid-span vertical displacement

Fig. 16. Effect of proportional distance and flange width on the steel beam.

V. Effects of the Upper-Floor Slabs

To assess the effect of an upper-floor slab on steel beams, a combined floor was built on the steel beam, and a 1/2 model was established during the FE analysis. The material, cell type, and grid size of the steel beams were maintained as the same, whereas the floor slab was designed as a combined slab with a thickness of 100 mm and width of 2500 mm. To

simplify the model, a plain steel plate made of Q355 steel with a thickness of 1 mm was selected. The force reinforcement was HRB400, the spacing was Φ2@200, the distribution bar was HPB300, the spacing was Φ6@300, and the concrete was C50. SHELL163 was used for the steel plates, BEAM161 for the reinforcing steel, and SOLID164 for the concrete, all with a mesh size of 50 mm. This section presents a comparative analysis of the failure processes of composite slabs and steel beams under different cases, as listed in Table V. Fig. 17 shows the FE model of a slab interacting with a beam.

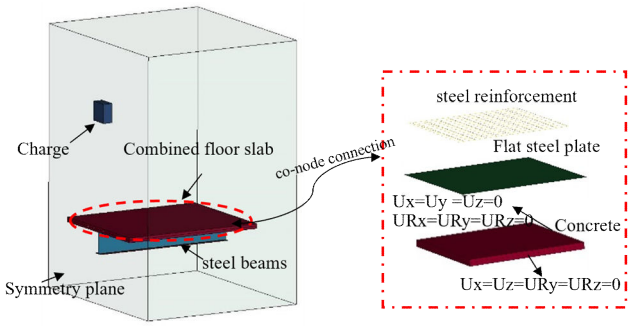

Fig. 17. Modelling of the steel beam and floor slab.

Fig. 18 shows the failure phenomena of the combined floor slabs under explosive loads under different working conditions. The explosion shock wave was transmitted to the floor slab, resulting in failure of the two ends of the concrete unit. The mid-span location of the concrete spatter indicates that the shorter the burst distance, the more obvious the degree of destruction of the center of the floor slab. The lower distribution reinforcement and steel plate fractured along the center position, leading to a significant failure of the floor over a large area. The beam collapsed along its length, resulting in shear failure at the ends of the floor and exposure of the ends of the steel beam. Additionally, some of the bearing bars failed and fractured, and one side of the steel plate sustained an M-shaped failure. Ultimately, the floor slab completely lost its ability to support weight.

Fig. 19 shows the maximum vertical displacements of the upper steel beam with and without floor slabs under the three working conditions. In the absence of a floor, the closer proximity of the explosives to the steel beam resulted in an increased vertical displacement. This phenomenon can be attributed to the intensification of the explosive shock wave as the distance from the explosion decreases. Consequently, the vertical displacements of the steel beam and slab increased as the distance from the explosion decreased. In the presence of an upper-floor slab, an increase in the proportional distance corresponded to a greater vertical displacement. The vertical displacement experienced in Case I, which accounted for the floor action, was significantly lower than that observed in the absence of floor action, with a reduction of 56.7%. In Cases II and III, the vertical displacement without the floor slab effect was smaller than that with the floor slab effect.

Fig. 20 shows the kinetic energy change in the upper-floor slab during the explosion, which explains this phenomenon. During the failure process, the upper slab fractured along the middle of the upper flange, allowing it to withstand higher potential impact energy. This resulted in debris falling. The steel beam on the upper floor dissipates most of the energy generated by the explosion, thereby providing a certain level of protection. As the proportional distance increased, the energy dissipation of the upper-floor slab decreased, resulting in the steel beam absorbing most of its energy. Consequently, the vertical displacement of the steel beams increased. Steel beams support floor slabs that function as flanges. This configuration increases the surface exposed to the explosion; therefore, for a certain proportional distance, when considering the floor effect, the vertical displacement is greater than the vertical displacement when there is no floor effect.

Fig. 21 illustrates the lateral displacements of the steel beams, both with and without the influence of slab action, across different scaled distances. The lateral displacement increased as the proximity to the bursting source decreased, whereas the overall lateral displacement with upper-floor action was smaller than that without floor action. The significant destruction of the upper-floor slab was primarily due to the reflection of the explosion shock wave from the steel beam, with a more pronounced effect correlated with the extent of failure. The presence of an upper-floor slab mitigated the instability of the steel beam and enhanced its lateral stiffness. Owing to the shattering of the upper-floor slab, the explosion shock wave reflected from the steel beam resulted in a greater degree of destruction and a more evident effect. The action of the upper-floor slab reduces the degree of instability of the steel beam and improves its lateral stiffness.

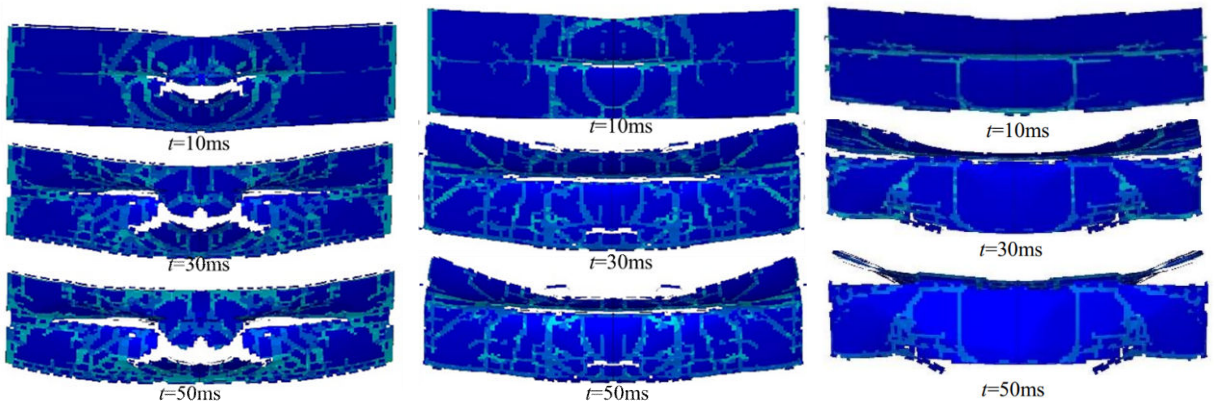

(a) CaseI (b) Case II (c) Case III

Fig. 18. Failure phenomena of combined floor slabs under different loading conditions

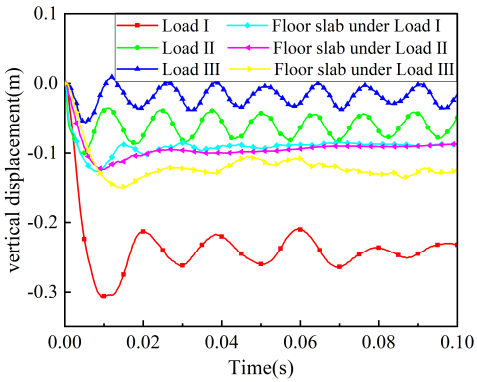

Fig. 19. Maximum vertical displacement of steel beams with and without upper-floor slab

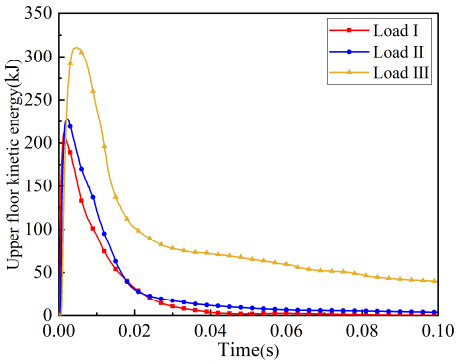

Fig. 20. Upper-floor kinetic energy

Fig. 21 illustrates the lateral displacements of the steel beams, both with and without the influence of slab action, across different scaled distances. The lateral displacement increased as the proximity to the bursting source decreased, whereas the overall lateral displacement with upper-floor action was smaller than that without floor action. The significant destruction of the upper-floor slab was primarily due to the reflection of the explosion shock wave from the steel beam, with a more pronounced effect correlated with the extent of failure. The presence of an upper-floor slab mitigated the instability of the steel beam and enhanced its lateral stiffness. Owing to the shattering of the upper-floor slab, the explosion shock wave reflected from the steel beam resulted in a greater degree of destruction and a more evident effect. The action of the upper-floor slab reduces the degree of instability of the steel beam and improves its lateral stiffness.

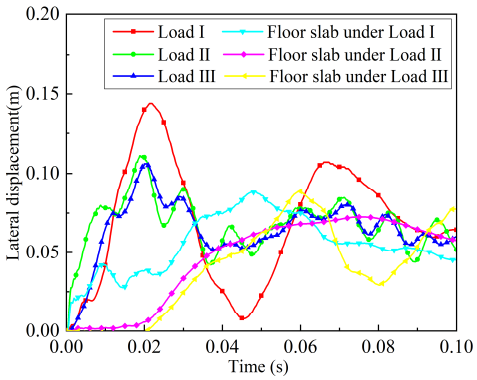

Fig. 21. Maximum lateral displacement of steel beams with and without upper-floor slab

Fig. 22 illustrates the equivalent stress clouds of steel beams under different conditions. Considering the influence of the upper-floor slab on the failure of the steel beams, the steel beams were subjected to uneven forces, the center location was subjected to large impacts, and flexural failure occurred. In Case I, out-of-plane instability occurred owing to the small proportional distance and evident shockwave flow. The lateral deflection decreased with increasing proportional distance and resulted in varying degrees of bending–torsion failure for each case.

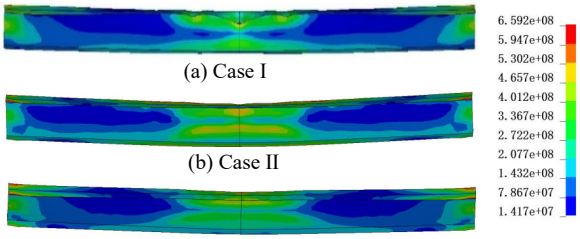

(a) Case I

(b) Case II

(c) Case III

Fig. 22. Equivalent stress of steel beams in different cases

VI. Conclusions

In this study, ANSYS/ LS-DYNA FE software was used to simulate and analyze the failure modes and dynamic responses of two-end fixed-support Q460 steel beams within a steel frame structure under the influence of a near explosion using the fluid–structure coupling method. The following conclusions were drawn from the analysis.

(1) The explosion generated shock waves that propagated spherically to the steel beam. These interacted with the steel beam, causing reflection and diffraction on its surface, resulting in maximum displacement and deflection at the midspan of the beam, along with significant lateral deformation, the energy absorbed by the flange is about twice that of the web. The pressure on the fixed supports at either end was substantial, and the peak pressure on these supports increased over time and spread evenly across the beam. A considerable plastic deformation was observed at the lower flange of the support.

(2) Welded composite I-shaped steel beams with fixed supports at both ends were subjected to different near-explosion loads at different scaled distances. When Z = 0.25 m/kg1/3, combined flexural and shear failure may occur; when Z = 0.38 m/kg1/3, local flange buckling failure may occur; when Z = 0.53 m/kg1/3, lateral flexural–torsion failure may occur. As the scaled distance decreases, the deformation of the steel beam increases and the degree of damage increases.

(3) Considering the combined effect of the upper floor on the steel beam, the degree of failure became more pronounced as the proportional distance decreased. In a composite floor, failure first occurred in the concrete, followed by collapse of the stressed reinforcement and steel plate in the floor along the beam direction, ultimately resulting in an M-shaped failure.

(4) As the proportional distance increased, the vertical displacement of the steel beam on the upper floor increased gradually, whereas the lateral displacement decreased. The presence of the upper floor had a protective effect when compared with no floor action, resulting in a 56.7% reduction in displacement and an increase in the bearing capacity of the steel beam. This ultimately led to a reduced risk of flexural and torsional failure.

REFERENCES

[1] Ban H, Shi G, "A review of research on high-strength steel structures," Proceedings of the Institution of Civil Engineers - Structures and Buildings, vol. 171, no. 8, pp 625-641, 2018.

[2] Cao T, Sun H, Zhou Y, Luo G, and Sun JW, "Numerical Simulation and Application of Propagation Characteristics of Shock Wave Near Ground Explosion," Journal of Ordnance Equipment Engineering, vol. 41, no. 12, pp 187-191, 2020.

[3] Xu JX, Liu XL, "Analysis of structural response under blast loads using the coupled SPH-FEM approach," Journal of Zhejiang University-SCIENCE A, vol. 9, no. 9, pp 1184-1192, 2008.

[4] Zhou J, Wang XG, An HM, Zhao MS, and Gong M, "The Analysis of Blasting Seismic Wave Passing Through Cavity Based on SPH-FEM Coupling Method," Engineering Letters, vol.27, no.1, pp 114-119,2019.

[5] Dinu F, Marginean I, Dubina D, Kovacs A, and Ghicioi E, "Experimental testing and numerical modeling of steel frames under close-in detonations," Procedia engineering, vol. 210, pp 377-385, 2017.

[6] Hu ZX, Li SQ, Liu ZH, Zhang P, Liu J, and Cheng YS, "Analysis on the bearing capacity and blast resistance of pressure stiffened double cylindrical shell structure," Chinese Journal of Ship Research, vol. 19, no. 3, pp 205-216, 2024.

[7] Zhao CF, Zhou ZH, Ye X, and Li XJ, "Numerical Study on Blast Resistance of Concrete-Infilled Double Steel Corrugated-Plate Wallboard Under Contact Explosion," Progress in Steel Building Structures, vol. 25, no. 12, pp 39-49, 2023.

[8] Hadianfard MA, Malekpour S, and Momeni M, "Reliability analysis of H-section steel columns under blast loading," Structural Safety, vol. 75, pp 45-56,2018.

[9] Momeni M, Bedon C, Hadianfard MA, and Baghlani A, "An Efficient Reliability-Based Approach for Evaluating Safe Scaled Distance of Steel Columns under Dynamic Blast Loads," Build, vol. 11, no. 12, pp 606, 2021.

[10] Momeni M, Hadianfard MA, Bedon C, and Baghlani A, "Damage evaluation of H-section steel columns under impulsive blast loads via gene expression programming," Engineering Structures, vol. 219, pp 110909 ,2020.

[11] Arafa IT, Elhosseiny OM, and Nawar MT, "Damage assessment of perforated steel beams subjected to blast loading," Structures, vol. 40, pp 646-658, 2022.

[12] Nawar MT, Arafa IT, and Elhosseiny OM, "Numerical damage evaluation of perforated steel columns subjected to blast loading," Defence Technology, vol. 18, no. 5, pp 735-746, 2022.

[13] Guruprasad S, Mukherjee A, "Layered sacrificial claddings under blast loading Part I analytical studies," International Journal of Impact Engineering, vol. 24, pp 957-973, 2000.

[14] Guruprasad S, Mukherjee A, "Layered sacrificial claddings under blast loading Part II experimental studies," International Journal of Impact Engineering, vol. 24, pp 975-984, 2000.

[15] Nassr AA, Razaqpur AG, Tait MJ, Campidelli M, and Foo S, "Single and multi-degree of freedom analysis of steel beams under blast loading," Nuclear Engineering and Design, vol. 242, pp 63-77, 2012.

[16] Nassr AA, Razaqpur AG, Tait MJ, Campidelli M, and Foo S, "Strength and stability of steel beam columns under blast load," International Journal of Impact Engineering, vol. 55, pp 34-48, 2013.

[17] Nassr AA, Razaqpur AG, and Campidelli M, "Effect of initial blast response on RC beams failure modes," Nuclear Engineering and Design, vol. 320, pp 437-451, 2017.

[18] Nassr AA, Razaqpur AG, Tait MJ, Campidelli M, and Foo S, "Dynamic Response of Steel Columns Subjected to Blast Loading," Journal of Structural Engineering, vol. 140, no. 7, pp. 04014036, 2014.

[19] Yang TC, Li GQ, Lu Y, and Chen SW, "Simplified Model for Analysis of Steel Frame Column Subjected to Blast Loading," Journal of Tianjin University (Science and Technology), vol. 50, no. 2, pp 188-197, 2017.

[20] Zhang CJ, Tan PJ, and Yuan Y, "Confined blast loading of steel plates with and without pre-formed holes," International Journal of Impact Engineering, vol. 163, pp 104183, 2022.

[21] Zhang XH, Zhang CW, and Duan ZD, "Numerical Simulation of Impact Response and Damage Mode of Steel Frame Columns under Explosive Loading," Journal of Shenyang Jianzhu University (Natural Science), vol. 25, no. 4, pp 656-662, 2009.

[22] Zhang XH, Lv CX, and Li YS, "Dynamic Response and Damage Analysis of Welded I-beam under Explosive Loads," Journal of Shenyang Jianzhu University (Natural Science), vol. 30, no. 3, pp 408-413, 2014.

[23] Zhang XH, Duan ZD, and Zhang CW, "Shock responses of steel frame structure near the ground explosion," Journal of Earthquake Engineering and Engineering Vibration, vol. 29, no. 4, pp 70-76, 2009.

[24] Zhou LY, Shi L, Xu LY, and Zhou ZH, "Method for Classifying Damage Level of Steel Column Under Impact of Explosion," Journal of Disaster Prevention and Mitigation Engineering, vol. 39, no. 5, pp 851-857, 2019.

[25] Nawar MT, Arafa IT, and Elhosseiny OM, "Numerical damage evaluation of perforated steel columns subjected to blast loading," Defence Technology, vol. 18, no. 5, pp 735-746, 2022.

[26] Arafa IT, Elhosseiny OM, and Nawar MT, "Damage assessment of perforated steel beams subjected to blast loading," Structures, vol. 40, pp 646-658, 2022.

[27] Hu ZJ, Li Y, Yu WS, and Fang JQ, "Anti-blast Resistance Analysis of Steel Box Girder under Close-by Blast," Blasting, vol. 36, no. 1, pp 117-125+154, 2019.

[28] Yu J, Liu FY, and Fang Q, "Distribution pattern and simplified model of blast load for building columns under near-field near-ground explosion," Explosions and shock waves, vol. 44, no. 1, pp 164-180, 2024.

[29] Xiao WF, Chen SQ, and Zhao XZ, "Numerical investigations of blast load distribution and dynamic response of I-shaped steel columns subjected to close-in explosions," Journal of Building Structures, vol. 45, no. 01, pp 12-26, 2024.

[30] An HM, Hou S, and Liu L, "Experimental and Numerical Study of the Concrete Stress and Fracture Propagation Processes by Blast," Engineering Letters, vol.27, no.4, pp 669-675, 2019.

[31] Nascimbene R, "Penalty partial reduced selective integration: a new method to solve locking phenomena in thin shell steel and concrete structures," Curved and Layered Structures, vol. 9, no. 1, pp 352-364, 2022.

[32] Shi SQ, "Engineering applications of ANASYS LS-DYNA in explosive and shock field," Beijing: China Architecture & Building Press, 2011.

[33] Zhang XH, Zhang WJ, and Zhang Y, "Dynamic response of Q460 high strength steel column under near explosion load," Journal of Vibration and Shock, vol. 41, no. 03, pp 107-114+147, 2022.

[34] Grisaro HY, Packer JA, and Seica MV, "Experimental and numerical investigation of bare and strengthened wide-flange sections subject to near-field blast loading," Journal of Structural Engineering, vol. 147, no. 9, pp 04021139, 2021.

[35] Zhang XH, "Experimental research and numerical simulation on blast resistance performance of steel frames Dissertation," Harbin: Harbin Institute of Technology, 2011.

[36] GB/T 50009-2012, "Load Code for Design of Building Structure," Beijing: China Standards Press, 2012.